ADVANCED MATERIALS
www.advmat.de

Single Quantum Dot Selection and Tailor-Made Photonic Device Integration using a Nanoscale-Focus Pinspot

Minho Choi, Mireu Lee, Sung-Yul L. Park, Byung Su Kim, Seongmoon Jun, Suk In Park, Jin Dong Song, Young-Ho Ko,* and Yong-Hoon Cho**

Among the diverse platforms of quantum light sources, epitaxially grown semiconductor quantum dots (QDs) are one of the most attractive workhorses for realizing quantum photonic technologies owing to their outstanding brightness and scalability. However, the spatial and spectral randomness of most QDs severely hinders the construction of large-scale photonic platforms. In this work, a methodology is presented to deterministically integrate single QDs with tailor-made photonic structures. A nondestructive luminescence picking method termed as nanoscale-focus pinspot (NFP) is applied using helium-ion microscopy to reduce the luminous QD density while retaining the surrounding medium. A single QD emission is only extracted out of the high-density ensemble QDs. Then the tailor-made photonic structure of a circular Bragg reflector (CBR) is designed and deterministically integrated with the selected QD. Given that the microscopy can image with nanoscale resolution and apply NFP in situ, photonic devices can be deterministically fabricated on target QDs. The extraction efficiency of the NFP-selected QD emission is improved by 25 times after the CBR integration. Since the NFP method only controls the luminescence without destroying the medium, it is applicable to various photonic structures such as photonic waveguides or photonic crystal cavities regardless of materials.

1. Introduction

Quantum light sources are essential building blocks for realizing quantum photonic technologies[1–6] and epitaxially grown semiconductor quantum dots (QDs)[7–31] are one of the most attractive platforms among various solid-state quantum light sources. These QDs are proving their potential as high-end quantum light sources with outstanding performance in terms of brightness, efficiency, purity, and indistinguishability as well as their integrability with optoelectronic devices.

The performance of these QDs can be drastically improved via photonic structure integration, and both spatial and spectral overlap between the QD and the optical mode of the photonic structure is essential.[12–25] However, the majority of QDs with cutting-edge performance are made by strain relaxation[13–28,31] or droplet epitaxy,[29,30] which results in a random location and emission wavelength of the QD. Therefore, to deterministically integrate the QD with a photonic structure, the location and emission wavelength of the QD must be measured and identified first, and then the appropriately designed photonic structure can be fabricated accordingly.

Confocal photoluminescence (PL) mapping and wide-field PL imaging techniques are the most representative methods in which both spatial and spectral information of QDs are measured simultaneously at high resolution.[20–24,31,32] However, it is difficult to identify a single QD when the density of the QD is too high; for instance, if multiple QDs are excited by a single focused laser beam, optical signals from those QDs can be measured at the same time, and

M. Choi[+], B. S. Kim, S. Jun, Y.-H. Cho
Department of Physics and KI for the NanoCentury
Korea Advanced Institute of Science and Technology (KAIST)
Daejeon 34141, Republic of Korea
E-mail: yhc@kaist.ac.kr

The ORCID identification number(s) for the author(s) of this article can be found under https://doi.org/10.1002/adma.202210667

[+]Present address: Department of Electrical and Computer Engineering, University of Washington, Seattle 98195, USA

DOI: 10.1002/adma.202210667

M. Lee, Y.-H. Ko
Quantum Technology Research Department
Electronics and Telecommunications Research Institute (ETRI)
Daejeon 34129, Republic of Korea
E-mail: yhko@etri.re.kr

M. Lee
Department of Physics
Ulsan Nation Institute of Science and Technology (UNIST)
Ulsan 44919, Republic of Korea

S.-Y. L. Park, S. I. Park, J. D. Song
Center for Opto-Electronic Materials and Devices Research
Korea Institute of Science and Technology (KIST)
Seoul 02456, Republic of Korea
E-mail: jdsong@kist.re.kr

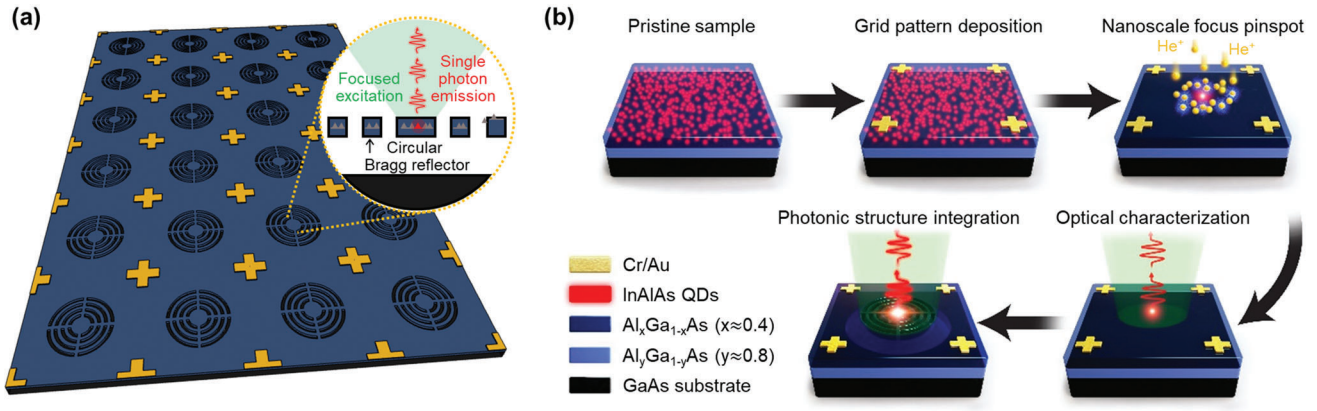

Figure 1. Concept of the deterministic integration of the selected QD with photonic structure. a) Schematics of site-selective single QD integrated with CBR structure. b) Procedures of a single QD selection from the ensemble QDs using NFP and deterministic fabrication with the CBR structure.

the information with respect to a single QD cannot be classified.

Hence, there have been a lot of efforts to form low-density QDs uniformly during the growth process, and there has been some success in a few material systems, including GaAs QDs grown by droplet epitaxy.[33] However, the formation of low-density QDs based on well-known Stranski–Krastanov (S–K) growth mode, such as In(Ga,Al)As on GaAs, III-N,[34] and III-Sb[35] QDs, remains a challenging issue. Although researchers intentionally create a density gradient along the wafer, the selected area of low-density part is limited.[28] Thus, it is difficult to expect homogenous properties from the QDs across the whole wafer, and the optical characterization and density estimation processes of the QD become more complicated. Moreover, low-density site-controlled QDs can be grown by the local strains,[36–38] nanohole arrays,[39,40] or local heating[41] on the wafer. However, the optical quality of these QDs are far short of the QDs naturally formed QDs after strain relaxation.

Hence, if the density of the QDs can be reduced after growing them and a single QD can be picked at the predetermined position, then it can lead to a sensational breakthrough for utilizing these high-density QDs from diverse material systems. Nanoscale patterning followed by mesa etching[22–24,32] and micrometer-scale metallic shadow masks[42,43] have been widely used to reduce QD density and separate a single QD. However, a critical issue arises for the mesa etching or metal deposition processes, in which integration with an on-chip photonic structure, i.e., photonic waveguide, photonic crystal cavity, and circular Bragg reflector (CBR), is no longer possible because all the materials surrounding the QD have already been etched or covered by the metals.

2. Results and Discussion

2.1. Nanoscale-Focus Pinspot (NFP) Technique

We developed a nondestructive nanoscale luminescence picking method utilizing focused-ion-beam (FIB) induced luminescence quenching and termed it as the nanoscale-focus pinspot (NFP).[8] Here, we use a helium-ion beam due to its high directionality inside the crystal structure.[44] Given that we can selectively quench unwanted emissions without destroying the photonic structure, this method can be an optimal solution for high-density QDs to reduce their luminous QD density and still enable them to integrate with photonic structures in the lateral direction.

In this study, we successfully reduced the luminous QD density from 40 to 1 μm^{-2} using the NFP technique and observed only a single QD emission among the ensemble QDs. The selected single QD location can be predetermined with respect to the metallic markers on the surface, and the QD can be deterministically integrated with photonic structures as shown in **Figure 1**a. We first measured the optical properties (i.e., emission wavelength and polarization) of the selected QD and then designed and fabricated a CBR accordingly. The extraction efficiency of the identical QD emission was improved 25 times after integration with the CBR structure.

Figure 1b shows a schematic of the entire process. A minimal reproducible density of self-assembled InAlAs/AlGaAs QD sample was grown via molecular beam epitaxy in the modified S–K growth mode.[45] The density of the QDs was estimated at ≈40 μm^{-2} via atomic force microscopy of the top QD layer (Section S1, Supporting Information). From around this density or higher, the formation of QDs are stable and reproducible. The metallic markers are formed on the sample surface via the lift-off process. Therefore, subsequent experiments of FIB irradiation, optical characterization, and CBR structure fabrication can be conducted according to the metallic markers. Given the FIB can image the metallic markers and perform the in situ NFP process, the reliability of the NFP process is approximately a few nanometers in scale. The most important advantage of this procedure is that the dimensions of the photonic structure can be determined with respect to the optical properties (i.e., wavelength and polarization direction) of the selected QD after the NFP process. Therefore, the spectral and spatial overlap between the QD and photonic structures can be determined deterministically.

2.2. Single QD Selection using the NFP Technique

During the NFP process, we used helium-ion microscopy (HIM), which has a higher quenching resolution than the conventional FIB using gallium ions. It is important to note that scanning

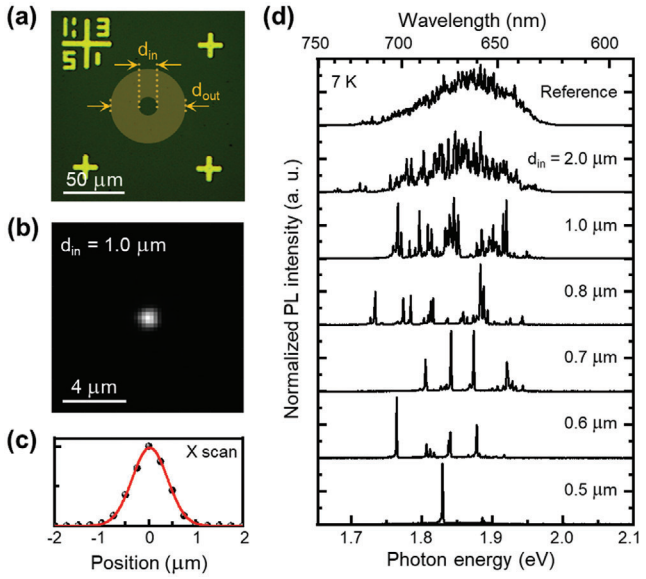

Figure 2. NFP process for a high-density ensemble QDs. a) Optical microscopy image of the metallic markers and a schematic of a doughnut-shaped helium-ion irradiation. b) Low-temperature micro-PL mapping of the NFP-processed emission. c) Line-scan of the micro-PL mapping for one QD. d) Inner diameter dependent micro-PL spectra of the QD emission after the NFP process.

electron microscopy (SEM) is not installed inside the HIM equipment, so it is difficult to image the sample with a helium-ion beam without causing luminescence quenching owing to ion bombardment. The following is the procedure for deterministic NFP process with respect to the markers. We first imaged only metallic markers by HIM, confirming the position of the center of those markers. Then, applied NFP at the center of the markers without imaging that particular area (detailed process is described at Section S2 in the Supporting Information). For the NFP process, we irradiated the helium-ion beam in a doughnut-shaped pattern with an outer diameter (d_{out}) of 20 μm and varied the inner diameter (d_{in}) from 0.5 to 5.0 μm (**Figure 2**a). We used 1.0×10^{14} cm^{-2} helium-ion irradiation dose condition to fully quench the QD emission where the HIM was irradiated (Section S3, Supporting Information). At this dose, we observed luminescence quenching followed by a doughnut-shaped irradiation pattern by measuring the low-temperature cathodoluminescence (CL) image (Section S4, Supporting Information). It should be noted that there were no imprints on the surface from the SEM image. Hence, we can integrate tailor-made photonic circuits for the chosen QD after measuring the optical properties of the QD after the NFP process because there is no structural destruction.

The optical properties of the luminous QDs at the center of the doughnut-shaped irradiation pattern were measured via low-temperature PL experiments at 7 K. We used a continuous-wave laser with a wavelength of 532 nm and an objective lens with a numerical aperture of 0.65 and magnification power of 50× for the optical measurement. Figure 2b shows the low-temperature micro-PL mapping result of the QD emission where the NFP process was performed with d_{in} of 1.0 μm. The mapping image represents a spatially resolved QD emission intensity, where all PL intensities of the QD emission from 640 to 720 nm were integrated. Based on the mapping image, we can observe the spotlighted QD emission after the NFP process, and the full width at half maximum (FWHM) of the bright spot is ≈0.750 ± 0.005 μm (Figure 2c), which is similar to the excitation laser beam spot. The PL mapping image of the QD layer without the NFP process is shown in Section S5 (Supporting Information), where QD emission is observed throughout. As shown in Section S5 (Supporting Information), we can apply NFP process in arrays or wherever we want according to the markers, therefore large-scale multiple QDs integrated system can be constructed. Figure 2d shows the micro-PL spectra of the bright spot after the NFP process as the d_{in} varies. When the d_{in} of the irradiation pattern decreases from 5.0 to 0.5 μm, the number of QD emission peaks decreases. Eventually, we obtained only a single QD peak after the NFP process when d_{in} was ≈0.5 μm. We can adjust the luminous region, not only a single emission spot, by simply adjusting the irradiation pattern. Moreover, the process can be done quite fast thanks to the extremely low dose condition for luminescence quenching, less than 10 s is taken for 100 μm^2. Hence, highly scalable integration with multiple QDs can be expected.

In addition, we estimate the number of luminescent QDs after the NFP process depend on the d_{in} of its irradiation pattern. From the CL image (Section S4, Supporting Information), we can treat the actual, or effective, luminescent region after the NFP process as 0.4 μm small than the d_{in}, following the equation, $d_{eff} = d_{in} - 0.4$ μm. Since we already know the density of the QDs, we can estimate the number of QDs remaining luminescent by multiplying the density and area, and the result is relevant to the number of peaks in low-temperature micro-PL spectra (Section S6, Supporting Information).

Furthermore, we undergo the same process on the self-assembled InAs/InP QDs which have emission wavelength in telecom O-band, and extract a single QD emission from the ensemble QDs (Figure S7, Supporting Information). In this regard, we can confirm that the NFP process is applicable for various solid-state QDs regardless of their material systems.

Figure 3 shows the optical characterization of the selected single QD emission after the NFP process. Here, we used a pulsed laser with a wavelength of 532 nm using the second-harmonic generation of a Ti:sapphire laser pumped optical parametric oscillator system. Figure 3a shows the highly resolved QD emission spectrum, where FWHM is ≈128 ± 2 μeV from the Voigt-functional fitting. Since we can only measure the ensemble QDs emission before the NFP process, we are not able to compare the linewidth of the identical QD emission before and after the NPF process. However, in a previous study, we have shown that the linewidth of the QD emission does not change after the NFP process from the site-controlled single QD emission.[8]

Figure 3b shows the power-dependent PL intensity of the QD emission. Specifically, the PL intensity represents the integrated QD emission spectra after Voigt-functional fitting. The power dependence follows the relationship: $I(P) = I_{sat}(1 - A\exp(-P/P_{sat}))$. We can clearly observe a one-to-one proportionality of the exciton emission at the lower excitation power region, and the emission intensity is saturated at the high excitation power region, I_{sat}, which corresponds to the brightness of the QD. Figure 3c shows the time-resolved PL signal of the single QD emission, and the lifetime is obtained as 835 ± 5 ps from the exponential decay functional fitting, $I(t) = I_0\exp(-t/\tau)$, where τ denotes the

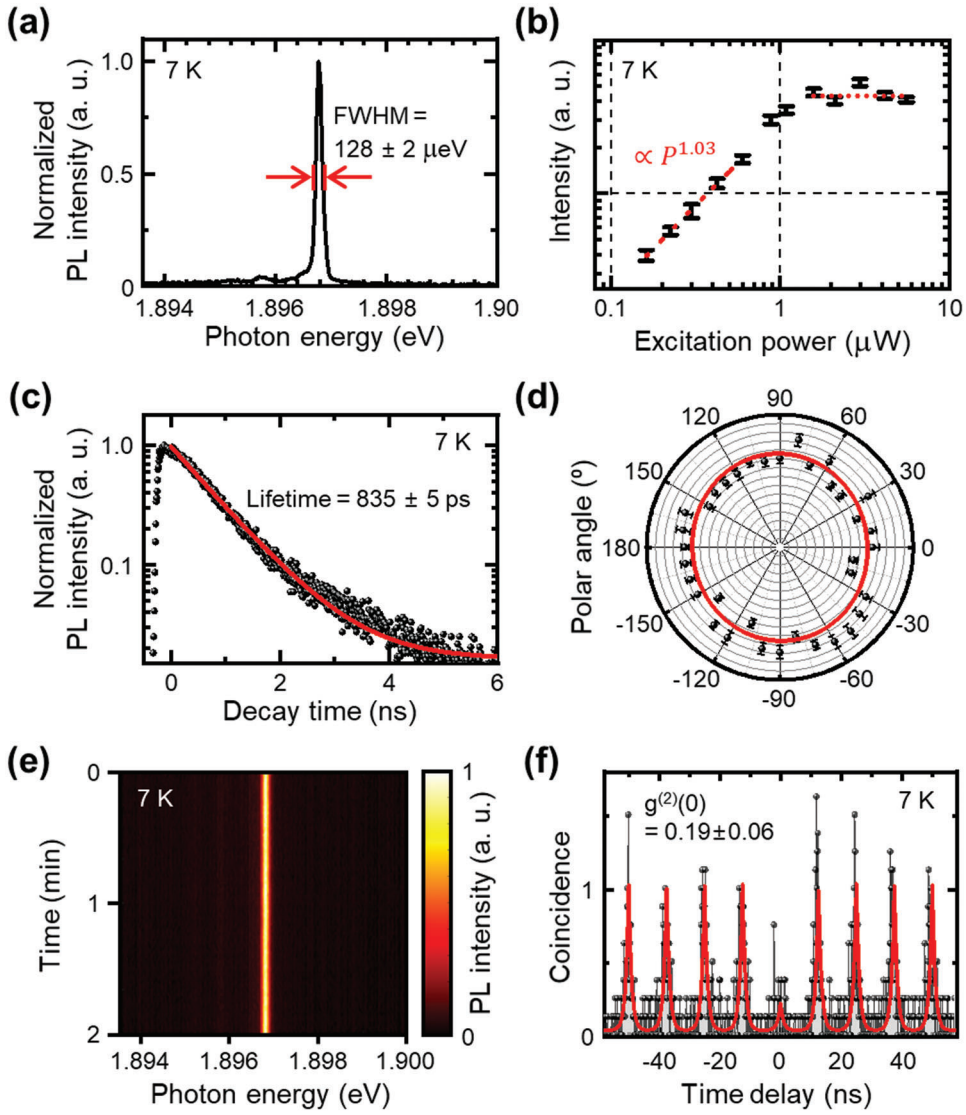

Figure 3. Optical characterization of a selected single QD after the NFP process. a) High-resolution micro-PL spectrum of a single QD emission. b) Power-dependent PL intensity of a single QD emission. c) Time-resolved PL intensity of a single QD emission. d) Polarization dependence of a single QD emission. e) Long timescale spectral diffusion of a single QD emission. f) Second-order photon correlation of a single QD emission.

lifetime. Figure 3d shows the linear polarization dependence of the single QD emission, and we can observe that there is no significant degree of linear polarization of the QD. A lot of photonic devices, i.e., waveguide, cavity, have certain mode corresponding to their wavelength and polarization direction. Hence, it is critical to figure out what is the emission wavelength and the polarization direction of the QD before designing and integrating the photonic structure accordingly. For the ensemble QDs, it is difficult to distinguish the single QD emission properties at desired position, because all the signal is contaminated by the adjacent QD emitters. On the contrary, we can measure those optical properties of a single selected QD after the NFP process. Moreover, we can apply magnetic field to the selected single QD after the NFP process to investigate the origin of the emission and the fine-structure splitting value (Section S8 (Supporting Information), for different QDs from Figure 3).[46]

Figure 3e shows the spectral diffusion of the quantum emission over a longer timescale compared to that of the linewidth. We measure the QD emission spectra 120 times with 1 s for each spectrum. We can clearly see that there is no blinking, and from the Voight-functional fitting of every 120 spectra, we can extract the standard deviation of the peak position and integrated intensity of the QD emission. As a result, the standard deviation of the emission energy was ≈2.0 μeV over 120 s, which is negligible compared to the spectral resolution of the measurement setup of ≈100 μeV. Also, the standard deviation of the integrated intensity of the QD emission is ≈1.8%. Hence, we can conclude that there is no degradation in the coherence properties of the QD emission after the NFP process in terms of short and long timescale.

Figure 3f shows the second-order photon correlation of the QD emission. Under pulsed-laser excitation, the correlation follows the formula $g^{(2)}(t) = \sum A_i \exp(-|t - t_i|/\tau)$, where t denotes the time

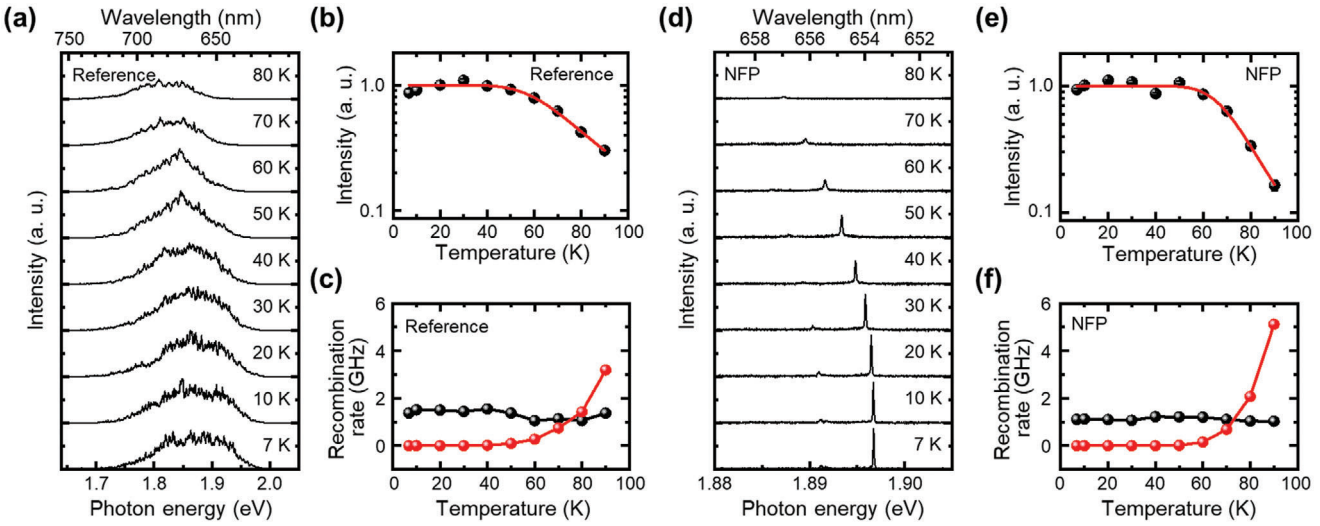

Figure 4. Temperature-dependent optical characterization of ensemble QDs and a single QD after the NFP process. a) Micro-PL spectra of ensemble QDs emission without the NFP process. b) Temperature-dependent PL intensity of ensemble QDs emission without the NFP process. c) Temperature-dependent radiative (black) and nonradiative (red) recombination rate of ensemble QDs emission without the NFP process. d) Micro-PL spectra of a selected single QD emission after the NFP process. e) Temperature-dependent PL intensity of a selected single QD emission after the NFP process. f) Temperature-dependent radiative (black) and nonradiative (red) recombination rate of a selected single QD emission after the NFP process.

delay and τ denotes the effective recombination time. The autocorrelation of the QD emission at zero time delay, $g^{(2)}(t = 0)$, is $\approx 0.19 \pm 0.06$. A value below 0.5 is evidence of a single-photon source. As shown in Figure 2d, we selected a single QD emission from the ensemble QD emission after the NFP process by measuring the spectrum. Here, we can confirm that the single QD emission is truly a single photon emission by measuring its autocorrelation. The single-photon purity of the QD emission is greater than 0.8 after the NFP process, and the remaining multiphoton events are less than 0.2. The measured single-photon purity can be further improved by optimizing the growth process (i.e., the absence of a wetting layer)[29] and optical characterization process (i.e., resonant excitation).[13]

2.3. Quantum Efficiency of the Selected QD from the NFP Technique

We successfully selected a single QD emission from high-density QDs and discussed its coherence properties. In **Figure 4**, we focus on the internal quantum efficiency of ensemble QDs and a single QD after the NFP process. Given that the NFP process selectively quenched the luminescence from undesired areas, there might be an influence of surrounding defects on the selected emitter. Therefore, we compared the temperature-dependent PL intensity and lifetime of the QD emissions before and after the NFP process. Before the NFP process, it was not possible to identify a single QD emission; therefore, we measured the ensemble QD emission at three different positions and statistically analyzed the results (Figure 4a–c). Furthermore, we identified a single QD emission after the NFP process; therefore, temperature-dependent PL intensity and lifetime were measured for a selected single QD after the NFP process of the doughnut irradiation with an inner diameter of 0.7 μm (Figure 4d–f). Additionally, we selected a few QD emissions using the mesa-etching process and measured the temperature-dependent PL (Section S9, Supporting Information) to compare the results with the NFP-processed QD.

Figure 4a,d shows the temperature-dependent micro-PL spectra of the ensemble QDs and single QD emissions before and after the NFP process, respectively. Correspondingly, Figure 4b shows the integrated PL intensity of all the ensemble QD emissions depending on their temperature, whereas Figure 4e shows the temperature dependence of the single QD emission intensity after the NFP. The results strongly follow the Arrhenius plot, $I(T) = I_0/(1 + A\exp(-E/k_B T))$, where E, k_B, and T denote the escape energy to the nonradiative channel, Boltzmann constant, and temperature, respectively. Based on the fitting, we can define and extract the effective internal quantum efficiency (QE_{eff}) as the relative emission intensity ratio of the QD between 70 and 7 K, $QE_{eff} = I_{70K}/I_{7K}$, and compare the values of the pristine ensemble QDs and single QD after the NFP and mesa-etching processes. The QE_{eff} value of the pristine ensemble QDs is ≈0.60 while the values of the single QD after the NFP and mesa-etching processes are 0.62 and 0.04, respectively (Section S9, Supporting Information). We can clearly observe that the internal quantum efficiency of the selected QD after the NFP process is significantly higher than that of the QD after the mesa-etching process. The large difference between the NFP and mesa-etching process is plausibly due to the absence of etched surface states after NFP.[47] Conversely, the QE_{eff} values of the single QD after the NFP process are almost similar to those of the pristine ensemble QDs; therefore, we can conclude that the NFP process does not affect the internal quantum efficiency of the selected QD emission, which is similar to the coherence property discussed in Figure 3.

To further investigate the carrier dynamics inside the single QD after the NFP process, we measured the time-resolved PL at different temperatures from 7 to 90 K (Figure 4c,f). We extracted radiative and nonradiative recombination rates from the measured lifetime using the following formula:

$k_{measured}(T) = k_{rad}(T) + k_{nonrad}(T)$; $k_{measured} = 1/\tau_{measured}$; IQE = $k_{rad}/(k_{rad} + k_{nonrad})$, where $k_{measured}$, k_{rad}, and k_{nonrad} denote the measured, radiative, and nonradiative recombination rates, $\tau_{measured}$ denotes the measured lifetime, and IQE denotes the internal quantum efficiency obtained from the temperature-dependent PL intensity (Figure 4b,e). Based on this formula, we can successfully separate the radiative and nonradiative recombination rates from the measured recombination rates at each temperature. The results show that the radiative recombination rate is almost constant at varying temperatures, which is a characteristic of 3D-confined QD emission, whereas the nonradiative recombination rate increases at elevated temperatures. Nonradiative recombination became dominant from 80 K for both nontreated reference QDs and single QD after the NFP process, which implies that there was no degradation of the QDs after the NFP process in terms of quantum efficiency and radiative carrier recombination process.

2.4. Tailor-Made Photonic Structure Integration with the Selected QD

We have shown that the NFP process enables the selection of a luminous single QD from high-density QDs and does not degrade its coherence properties and quantum efficiency. Above all those advantages, structural nondestructiveness is the most important aspect of the NFP process wherein on-chip integration is still available unlike the mesa etching process. Here, we demonstrate the deterministic integration of a selected single QD with a CBR following the procedure above (Figure 1b). Here, the sample has AlGaAs sacrificial layer of high-Al contents, we can selectively wet etch the layer and form a free-standing structure (Section S10, Supporting Information). Given that we know the position of the NFP-processed QD with respect to the markers, we are able to realize a spatial overlap between the QD and photonic structure. Additionally, the optical properties of the selected QD after the NFP process can be measured first, followed by the design and fabrication of the tailor-made photonic structure for the selected QD can be performed afterward; therefore, the spectral overlap between the QD and photonic structure can be realized (Section S12, Supporting Information).

Specifically, we selected the CBR structure for integration with the selected QD after NFP. The CBR structure was adopted for various quantum emitters to improve their extraction efficiency.[48,49] In most cases, these QDs are surrounded by a high-refractive-index medium; therefore, a large portion of the emission cannot escape the host medium and is difficult to be collected by free-space optical systems. Hence, we measured the brightness of the identical single QD emission before and after CBR structure integration and determined the improvements of the extraction efficiency after integration. CBR is fabricated by the following process: after the NFP process and optical characterization, aligned electron-beam lithography with respect to the metallic markers followed by reactive ion etching with chlorine-based gases, and the wet etching undercut process using HF solution provides a freestanding CBR structure that contains the selected QD at the center.

Figure 5a shows an SEM image of the freestanding AlGaAs CBR containing InAlAs QDs. Figure 5b shows the simulated far-field irradiation pattern of the QD coupled with the CBR structure, while the inset image shows the result from the QD before CBR fabrication. Highly directional Gaussian-like irradiation from the QD coupled with the CBR structure can be observed, which clearly differs from the QD inside a planar structure. Figure 5c shows the simulated extraction efficiency of the QD emission with respect to the numerical aperture (NA) of the collecting optics. The calculated extraction efficiency of the QD coupled with the CBR structure is ≈0.44 with a collecting system of NA 0.65 that we used. This can be doubled when we collect upward and downward emissions by implementing a reflector at the bottom, i.e., a distributed Bragg reflector. For comparison, the calculated extraction efficiency of a single QD in a slab structure before fabricating the CBR structure was ≈0.0053. Therefore, the extraction efficiency of the QD emission was enhanced by ≈80 times with CBR coupling.

Figure 5d shows the micro-PL spectra of the selected single QD after the NFP process with and without CBR structure integration under the same excitation condition with a 532-nm pulsed laser at 7 K. By comparing the optical properties of an identical QD before and after the CBR structure, it is straightforward to discuss about the extraction efficiency enhancement after CBR structure integration. Here, we precisely verify and calibrate the optical measurement setup between two measurements of before and after CBR structure fabrication by measuring the reference QD sample (Section S13, Supporting Information). Therefore, we can clearly conclude that the intensity of the QD emission is significantly improved owing to coupling with the CBR structure (Figure 5d). From the 2 × 2 arrays of selected QDs, separated by 14 μm to each other, we successfully integrated those QDs with tailor-made CBR structures and they all showed significant PL intensity enhancement up to 80 times (Section S13, Supporting Information). The different enhancement factor between each selected QDs can be originated by the different CBR designs at the QD emission wavelength (Section S12, Supporting Information). We can also notice that the peak position of the QD coupled with the CBR structure undergoes a redshift, and it is expected to be due to the strain change on the QD with the freestanding structure.

Figure 5e shows the PL peak intensity of the QD emission before and after the CBR structure integration. In order to focus on the extraction efficiency of the fabricated CBR structure and rule out the other factors, i.e., field localization and lifetime, we measured the pulse excitation and power-dependence of the PL emission and look into the saturated intensity. After the CBR integration, the PL intensity will vary at low excitation power due to the Purcell enhancement, but at saturated intensity, we can compare only the extraction efficiency before and after the CBR structure integration. Then we measured lifetime directly from the time-resolve PL. In Figure 5e, we fitted the power-dependent PL intensity with the following function, $I(P) = I_{sat}(1 - A\exp(-P/P_{sat}))$, the saturated intensity I_{sat}, which corresponds to the brightness of the QD emission, was enhanced by 29.5 times (from 190 to 5610) and 24.8 times after the calibration. The enhancement factor is of the same order as the calculated value of 80, whereas some difference may be originated from an imperfection of designed fabrication. For the other selected QDs in the 2 × 2 arrays, we also achieved the average enhancement factor as 11.2 (Section S13, Supporting Information).

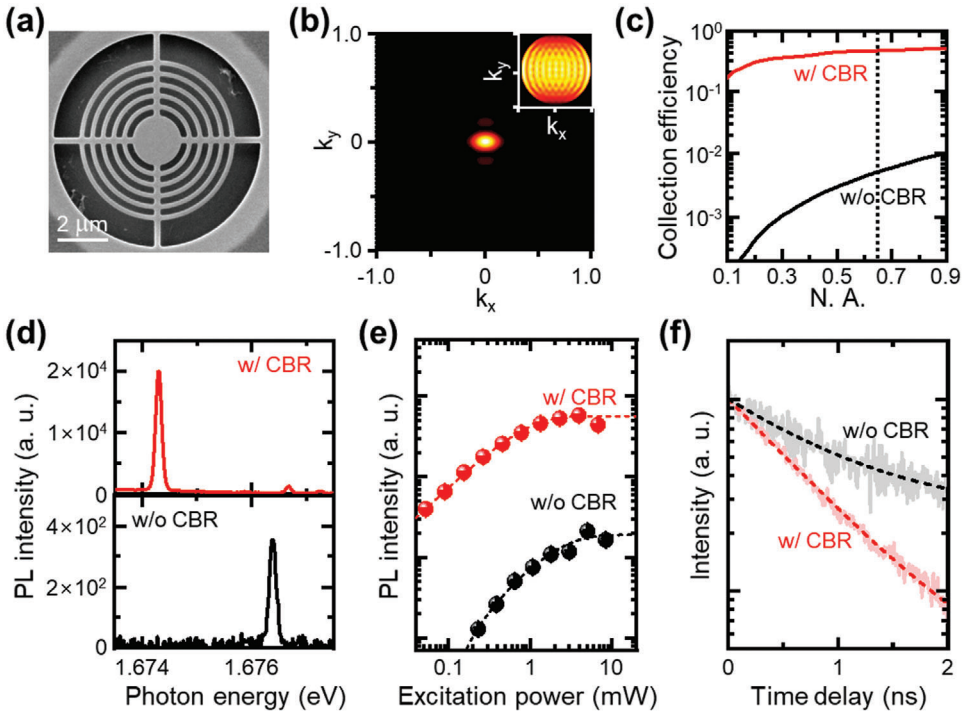

Figure 5. Deterministic integration between a selected single QD after the NFP process and a CBR. a) SEM image of a CBR. b) Optical simulation of a far-field irradiation pattern of a single QD in a CBR structure. The inset image denotes the far-field irradiation pattern of a single QD in a slab structure. c) Calculated extraction efficiency of a single QD in a CBR structure and a slab structure. d) Low-temperature micro-PL spectra of an identical single QD emission before and after the CBR integration. Note that the *y*-axis scales are different for two cases. e) Power-dependent PL intensity of the identical single QD selected by the NFP process before and after the CBR integration. f) Time-resolved PL intensity of the identical single QD selected by the NFP process before and after the CBR integration.

The results clearly show the deterministic integration of this method.

Figure 5f shows the time-resolved PL intensity of the QD emission before and after the CBR structure integration. From the exponential functional fitting, the lifetime of the QD emission before and after the integration has measured as 940 and 720 ps, respectively. Here, the QD emission is measured under low-temperature, and the QD is far apart from the etched surface, therefore we can consider the measured lifetime as a radiative term. Therefore, the radiative recombination rate enhancement, so called Purcell enhancement, has measured as a factor of 1.3. This value is much lower than the common photonic cavity structures with high quality factors and small mode volume. However, we designed the CBR structure as optimized for high directionality with large mode effective mode are of about $(0.7/\lambda)^2$. As a result, the expected Purcell enhancement factor is around 9–15 (Section S11, Supporting Information), and the value is not much difference from the measured value of 1.3. The ensemble QDs, without the NFP process, also shows the Purcell enhancement factor from 1.1 to 2.2 after integrating with CBR structures (Section S14, Supporting Information).

Moreover, we can crosscheck the measured Purcell enhancement factor from the measured PL intensity and brightness of the identical QD before and after the CBR structure integration. At the same excitation laser power, the Purcell factor can be understood as the local enhancement of excitation field.[50] Therefore, the effective excitation power density is enlarged under Purcell enhancement. And at the low-excitation power regime, the QD emission intensity is linearly proportional to the excitation power. Hence, we can setup the measured PL intensity as the following equation, $I_{CBR}/I_0 = (\eta_{CBR}/\eta_0) \times (\tau_0/\tau_{CBR})$, where the η and τ are the extraction efficiency and lifetime. From the 2×2 arrays of selected QDs, an average of the measured PL intensity ratio, I_{CBR}/I_0 is about 24.8, while the measured extraction efficiency enhancement and the Purcell factor are about 11.2 and 1.64, we can verify the measured values are plausible.

3. Conclusion

We have developed the effective and scalable method for building low-density and site-controlled quantum emitters by utilizing FIB-induced luminescence quenching. This NFP process enables single-QD selection from high-density ensemble QD emission without degrading its coherence properties and quantum efficiency. Having a single QD at the predetermined position is an important asset for large scale quantum photonic technologies. Also reducing the QD density can provide more room for diverse material systems, and alleviate the epitaxially growth conditions. Most importantly, the NFP process does not destroy its surrounding medium and only selectively quenches its luminescence site. Therefore, on-chip integration includes not only a CBR, but also waveguides and photonic crystal cavities available after the NFP process. When the size of the optical interaction between the QD and circuit becomes larger, the meaningfulness

of the NFP process increases. For the deterministic integration, hybrid integration between the prefabricated photonic structures and the selected QDs using pick-and-place techniques are widely adopted.[51] However, there always exist the coupling loss issues, and the it is not well-suited for large-scale integration with hundreds and thousands number of QDs. In our work, by using the NFP process, we can provide arrays of selected QDs at any position regarding to the premade markers. Hence, we can create a large-scale multiple QDs integrated photonic circuits by using this technique.

Supporting Information

Supporting Information is available from the Wiley Online Library or from the author.

Acknowledgements

This work was supported by the National Research Foundation (2022R1A2B5B03002560 and 2020M3E4A1080112) and Institute of Information & Communications Technology Planning & Evaluation (2020-0-00841) of the Korean government, and the Samsung Science and Technology Foundation under Project Number SSTF-BA1602-05. The authors appreciate KAIST Analysis center for Research Advancement and DGIST CCRF for supporting experiments.

Conflict of Interest

The authors declare no conflict of interest.

Data Availability Statement

The data that support the findings of this study are available from the corresponding author upon reasonable request.

Keywords

photonic cavity integration, quantum dots, quantum light sources, semiconductor quantum dots, single photon sources

Received: November 16, 2022
Revised: February 20, 2023
Published online: May 5, 2023

[1] B. Ndagano, H. Defienne, D. Branford, Y. D. Shah, A. Lyons, N. Westerberg, E. M. Gauger, D. Faccio, *Nat. Photonics* **2022**, *16*, 384.
[2] B. Li, Y. Cao, Y. H. Li, W. Q. Cai, W. Y. Liu, J. G. Ren, S. K. Liao, H. N. Wu, S. L. Li, L. Li, N. L. Liu, C. Y. Lu, J. Yin, Y. A. Chen, C. Z. Peng, J. W. Pan, *Phys. Rev. Lett.* **2022**, *128*, 170501.
[3] T. Dai, Y. Ao, J. Bao, J. Mao, Y. Chi, Z. Fu, Y. You, X. Chen, C. Zhai, B. Tang, Y. Yang, Z. Li, L. Yuan, F. Gao, X. Lin, M. G. Thompson, J. L. O'Brien, Y. Li, X. Hu, Q. Gong, J. Wang, *Nat. Photonics* **2022**, *16*, 248.
[4] C. Vigliar, S. Paesani, Y. Ding, J. C. Adcock, J. Wang, S. Morley-Short, D. Bacco, L. K. Oxenløwe, M. G. Thompson, J. G. Rarity, A. Laing, *Nat. Phys.* **2021**, *17*, 1137.
[5] S. L. Severin Daiss, S. Welte, E. Distante, P. Thomas, L. Hartung, O. Morin, G. Rempe, *Science* **2021**, *317*, 614.
[6] L.-Z. Liu, Y.-Z. Zhang, Z.-D. Li, R. Zhang, X.-F. Yin, Y.-Y. Fei, L. Li, N.-L. Liu, F. Xu, Y.-A. Chen, J.-W. Pan, *Nat. Photonics* **2020**, *15*, 137.
[7] M. Choi, S. Kim, S. Choi, Y.-H. Cho, *Appl. Phys. Lett.* **2021**, *119*, 034001.
[8] M. Choi, S. Jun, K. Y. Woo, H. G. Song, H. S. Yeo, S. Choi, D. Park, C. H. Park, Y. H. Cho, *ACS Nano* **2021**, *15*, 11317.
[9] S. Gyger, J. Zichi, L. Schweickert, A. W. Elshaari, S. Steinhauer, S. F. Covre da Silva, A. Rastelli, V. Zwiller, K. D. Jons, C. Errando-Herranz, *Nat. Commun.* **2021**, *12*, 1408.
[10] H.-S. Yeo, K. Lee, J.-H. Cho, S.-H. Park, Y.-H. Cho, *Nano Lett.* **2020**, *20*, 8461.
[11] R. Uppu, L. Midolo, X. Zhou, J. Carolan, P. Lodahl, *Nat. Nanotechnol.* **2021**, *16*, 1308.
[12] A. Lyasota, C. Jarlov, M. Nyman, A. Miranda, M. Calic, B. Dwir, A. Rudra, A. Shevchenko, E. Kapon, *Phys. Rev. X* **2022**, *12*, 021042.
[13] L. Dusanowski, C. Nawrath, S. L. Portalupi, M. Jetter, T. Huber, S. Klembt, P. Michler, S. Hofling, *Nat. Commun.* **2022**, *13*, 748.
[14] A. Brooks, X. L. Chu, Z. Liu, R. Schott, A. Ludwig, A. D. Wieck, L. Midolo, P. Lodahl, N. Rotenberg, *Nano Lett.* **2021**, *21*, 8707.
[15] R. Uppu, F. T. Pedersen, Y. Wang, C. T. Olesen, C. Papon, X. Zhou, L. Midolo, S. Scholz, A. D. Wieck, A. Ludwig, *Sci. Adv.* **2020**, *6*, eabc8268.
[16] R. Uppu, H. T. Eriksen, H. Thyrrestrup, A. D. Ugurlu, Y. Wang, S. Scholz, A. D. Wieck, A. Ludwig, M. C. Lobl, R. J. Warburton, P. Lodahl, L. Midolo, *Nat. Commun.* **2020**, *11*, 3782.
[17] F. T. Pedersen, Y. Wang, C. T. Olesen, S. Scholz, A. D. Wieck, A. Ludwig, M. C. Löbl, R. J. Warburton, L. Midolo, R. Uppu, P. Lodahl, *ACS Photonics* **2020**, *7*, 2343.
[18] T. Huber, M. Davanco, M. Müller, Y. Shuai, O. Gazzano, G. S. Solomon, *Optica* **2020**, *7*, 380.
[19] N. Tomm, A. Javadi, N. O. Antoniadis, D. Najer, M. C. Lobl, A. R. Korsch, R. Schott, S. R. Valentin, A. D. Wieck, A. Ludwig, R. J. Warburton, *Nat. Nanotechnol.* **2021**, *16*, 399.
[20] B. Chen, Y. Wei, T. Zhao, S. Liu, R. Su, B. Yao, Y. Yu, J. Liu, X. Wang, *Nat. Nanotechnol.* **2021**, *16*, 302.
[21] T. Pregnolato, X. L. Chu, T. Schröder, R. Schott, A. D. Wieck, A. Ludwig, P. Lodahl, N. Rotenberg, *APL Photonics* **2020**, *5*, 086101.
[22] S. C. Wein, J. C. Loredo, M. Maffei, P. Hilaire, A. Harouri, N. Somaschi, A. Lemaître, I. Sagnes, L. Lanco, O. Krebs, A. Auffèves, C. Simon, P. Senellart, C. Antón-Solanas, *Nat. Photonics* **2022**, *16*, 374.
[23] H. Ollivier, I. Maillette de Buy Wenniger, S. Thomas, S. C. Wein, A. Harouri, G. Coppola, P. Hilaire, C. Millet, A. Lemaître, I. Sagnes, O. Krebs, L. Lanco, J. C. Loredo, C. Antón, N. Somaschi, P. Senellart, *ACS Photonics* **2020**, *7*, 1050.
[24] Y. Wei, S. Liu, X. Li, Y. Yu, X. Su, S. Li, X. Shang, H. Liu, H. Hao, H. Ni, S. Yu, Z. Niu, J. Iles-Smith, J. Liu, X. Wang, *Nat. Nanotechnol.* **2022**, *17*, 470.
[25] F. Sbresny, L. Hanschke, E. Scholl, W. Rauhaus, B. Scaparra, K. Boos, E. Zubizarreta Casalengua, H. Riedl, E. Del Valle, J. J. Finley, K. D. Jons, K. Muller, *Phys. Rev. Lett.* **2022**, *128*, 093603.
[26] T. Jin, X. Li, R. Liu, W. Ou, Y. Zhu, X. Wang, J. Liu, Y. Huo, X. Ou, J. Zhang, *Nano Lett.* **2022**, *22*, 586.
[27] J. Kettler, N. Vaish, L. M. de Lepinay, B. Besga, P. L. de Assis, O. Bourgeois, A. Auffeves, M. Richard, J. Claudon, J. M. Gerard, B. Pigeau, O. Arcizet, P. Verlot, J. P. Poizat, *Nat. Nanotechnol.* **2021**, *16*, 283.
[28] N. Bart, C. Dangel, P. Zajac, N. Spitzer, J. Ritzmann, M. Schmidt, H. G. Babin, R. Schott, S. R. Valentin, S. Scholz, Y. Wang, R. Uppu, D. Najer, M. C. Lobl, N. Tomm, A. Javadi, N. O. Antoniadis, L. Midolo, K. Muller, R. J. Warburton, P. Lodahl, A. D. Wieck, J. J. Finley, A. Ludwig, *Nat. Commun.* **2022**, *13*, 1633.
[29] L. Zhai, M. C. Lobl, G. N. Nguyen, J. Ritzmann, A. Javadi, C. Spinnler, A. D. Wieck, A. Ludwig, R. J. Warburton, *Nat. Commun.* **2020**, *11*, 4745.

[30] M. C. Lobl, C. Spinnler, A. Javadi, L. Zhai, G. N. Nguyen, J. Ritzmann, L. Midolo, P. Lodahl, A. D. Wieck, A. Ludwig, R. J. Warburton, *Nat. Nanotechnol.* **2020**, *15*, 558.
[31] Z. X. Koong, M. Cygorek, E. Scerri, T. S. Santana, S. I. Park, J. D. Song, E. M. Gauger, B. D. Gerardot, *Sci. Adv.* **2022**, *8*, eabm8171.
[32] S. Liu, K. Srinivasan, J. Liu, *Laser Photonics Rev.* **2021**, *15*, 2100223.
[33] M. Gurioli, Z. Wang, A. Rastelli, T. Kuroda, S. Sanguinetti, *Nat. Mater.* **2019**, *18*, 799.
[34] S. Tamariz, G. Callsen, N. Grandjean, *Appl. Phys. Lett.* **2019**, *114*, 082101.
[35] M. Baik, J. Kyhm, H.-K. Kang, K.-S. Jeong, J. S. Kim, M.-H. Cho, J. D. Song, *Sci. Rep.* **2021**, *11*, 7699.
[36] J. Große, M. von Helversen, A. Koulas-Simos, M. Hermann, S. Reitzenstein, *APL Photonics* **2020**, *5*, 096107.
[37] J. Zhang, S. Chattaraj, S. Lu, A. Madhukar, *Appl. Phys. Lett.* **2019**, *114*, 071102.
[38] K. D. Jons, P. Atkinson, M. Muller, M. Heldmaier, S. M. Ulrich, O. G. Schmidt, P. Michler, *Nano Lett.* **2013**, *13*, 126.
[39] S. Kiravittaya, M. Benyoucef, R. Zapf-Gottwick, A. Rastelli, O. G. Schmidt, *Appl. Phys. Lett.* **2006**, *89*, 233102.
[40] C. Schneider, A. Huggenberger, M. Gschrey, P. Gold, S. Rodt, A. Forchel, S. Reitzenstein, S. Hofling, M. Kamp, *Phys. Status Solidi A* **2012**, *209*, 2379.
[41] Y. R. Wang, I. S. Han, C. Y. Jin, M. Hopkinson, *ACS Appl. Nano Mater.* **2020**, *3*, 4739.
[42] C. Salter, R. Stevenson, I. Farrer, C. Nicoll, D. Ritchie, A. Shields, *Nature* **2010**, *465*, 594.
[43] R. M. Stevenson, R. J. Young, P. Atkinson, K. Cooper, D. A. Ritchie, A. J. Shields, *Nature* **2006**, *439*, 179.
[44] V. V. Gregor Hlawacek, R. van Gastel, B. Poelsema, *J. Vac. Sci. Technol. B* **2014**, *32*, 020801.
[45] S. Y. Kim, J. D. Song, I. K. Han, T. W. Kim, *J. Nanosci. Nanotechnol.* **2014**, *14*, 5881.
[46] B. Witek, R. Heeres, U. Perinetti, E. Bakkers, L. Kouwenhoven, V. Zwiller, *Phys. Rev. B* **2011**, *84*, 195305.
[47] J. Liu, K. Konthasinghe, M. Davanco, J. Lawall, V. Anant, V. Verma, R. Mirin, S. Woo Nam, J. Dong Song, B. Ma, Z. Sheng Chen, H. Qiao Ni, Z. Chuan Niu, K. Srinivasan, *Phys. Rev. Appl.* **2018**, *9*, 064019.
[48] H. Wang, Y.-M. He, T. H. Chung, H. Hu, Y. Yu, S. Chen, X. Ding, M. C. Chen, J. Qin, X. Yang, R.-Z. Liu, Z. C. Duan, J. P. Li, S. Gerhardt, K. Winkler, J. Jurkat, L.-J. Wang, N. Gregersen, Y.-H. Huo, Q. Dai, S. Yu, S. Höfling, C.-Y. Lu, J.-W. Pan, *Nat. Photonics* **2019**, *13*, 770.
[49] M. D. Eisaman, J. Fan, A. Migdall, S. V. Polyakov, *Rev. Sci. Instrum.* **2011**, *82*, 071101.
[50] S. I. Maslovski, C. R. Simovski, *Nanophotonics* **2018**, *8*, 429.
[51] J. H. Kim, S. Aghaeimeibodi, C. J. K. Richardson, R. P. Leavitt, D. Englund, E. Waks, *Nano Lett.* **2017**, *17*, 7394.